文章编号：1001-9014(XXXX)XX-0001-10

DOI:10.11972/j.issn.1001-9014.XXXX.XX.001

Modified Multiple-Component Scattering Power Decomposition for PolSAR Data based on Eigenspace of Coherency Matrix

ZHANG Shuang[1,2*], WANG Lu[1,3], WANG Wen-Qing[1,2,3]

(1. School of Automation and Information Engineering, Xi'an University of Technology, Xi'an 710048, P. R. China;
2. Xi'an Key Laboratory of Wireless Optical Communication and Network Research, Xi'an 710048, P. R. China;
3. Key Laboratory of Cognitive Radio and Information Processing, Ministry of Education, Guilin University of Electronic Technology, Guilin 541004, P. R. China)

Abstract: A modified multiple-component scattering power decomposition for analyzing polarimetric synthetic aperture radar (PolSAR) data is proposed in this letter. The modified decomposition involves two distinct steps. Firstly, eigenvectors of the coherency matrix are used to modify the scattering models. Secondly, the entropy and anisotropy are used to improve the volume scattering power. With the guarantee of high double-bounce scattering power in the urban areas, the proposed algorithm effectively improves the volume scattering power of vegetation areas. The efficacy of the modified multiple-component scattering power decomposition is validated using actual AIRSAR PolSAR data. The scattering powers obtained through decomposing the original coherency matrix and the coherency matrix after orientation angle compensation are compared with three algorithms. Results from the experiment demonstrate that the proposed decomposition yields more effective scattering powers for representing the PolSAR dataset.

Key words: PolSAR data, model-based decomposition, eigenvalue decomposition, scattering powers
PACS:

基于相干矩阵特征空间的改进PolSAR数据多元散射能量分解方法

张 爽[1,2*], 王 璐[1,3], 王文卿[1,2,3]

(1. 西安理工大学 自动化与信息工程学院,陕西 西安,710048;
2. 西安市无线光通信与网络研究重点实验室,陕西 西安,710048;
3. 桂林电子科技大学 认知无线电与信息处理省部共建教育部重点实验室, 广西 桂林, 541004)

摘要:本文提出了一种改进的极化合成孔径雷达(PolSAR)数据多元散射能量分解方法。改进后的分解方法包括两个不同的步骤。首先,利用相干矩阵的特征向量对散射模型进行修正;其次,利用熵和各向异性来提高体散射能量。该算法在保持城市区域中较高的二次反射散射能量的前提下,有效地提高了植被区域的体散射能量。利用真实的数据验证了本文方法的有效性。将原始相干矩阵分解得到的散射能量和方向角补偿后得到的相干矩阵分解的散射能量与三种已有的分解算法进行了对比。实验结果表明,本文提出的分解方法能够更有效地表示不同地物的极化SAR数据集的散射能量。

关 键 词:极化SAR数据;模型分解;特征值分解;散射能量

I Introduction

Because of all-time, all-weather, and multi-band imaging characteristics, polarimetric synthetic aperture radar (PolSAR) has become widely used in various application areas. In recent years, various new PolSAR sensors have been launched and various PolSAR missions have been carried out, resulting in an increase in the amount of data requiring interpretation and processing. Target decomposition has emerged as the primary approach for interpretation and preprocessing due to its ease of implementation and strong physical meaning. For PolSAR images, target decomposition methods can be

Foundation items: Supported by the National Natural Science Foundation of China (No. 62376214), the Natural Science Basic Research Program of Shaanxi (No. 2023-JC-YB-533) and Key Laboratory of Cognitive Radio and Information Processing, Ministry of Education (No. CRKL200203).

Biography: Zhang Shuang (1983-), female(Manzu), jinzhou, Ph. D., lecturer at Xi'an University of Technology. Research area involves PolSAR data interpretation and processing, and deep learning in the complicated data.

* **Corresponding author**: E-mail: shzhang_work@163.com.

categorized into two groups: model-based decomposition [1-14] and eigenvalue-based decomposition [15-22].

In 1998, Freeman and Durden introduced the Freeman-Durden decomposition (FDD) [1], which is a classical model-based decomposition method. FDD involves decomposing the covariance matrix of PolSAR data into three main components: surface scattering, double-bounce scattering and volume scattering. Although FDD has efficiently described the physical features of PolSAR data, it has a major shortcoming in that there are negative surface and double-bounce scattering powers. This is due to the assumption of reflection symmetry theory, where the co-polarized term is uncorrelated with the cross-polarized term resulting in T_{13} and T_{23} being zero in the coherency matrix ($[T]$). As a result, the cross-polarized power only contributes to the volume scattering component, causing the volume scattering power to be overestimated and possibly greater than the total power. It leads to negative surface and double-bounce scattering powers.

There are three primary methods for enhancing FDD. The first technique involves performing orientation angle compensation (OAC) on the coherency matrix or the covariance matrix of the POLSAR data prior to decomposition [2][3][4]. By orienting the coherency or covariance matrix in this way, the cross-polarized power is reduced, resulting in a smaller volume scattering power. Consequently, the number of negative surface scattering and double-bounce scattering powers is also reduced. The second strategy for improving FDD is to optimize the scattering models, particularly the volume scattering model or by introducing a new scattering model that shares the crossed-polarized power with the volume scattering [5-14]. For example, Yamaguchi introduced the helix scattering model as the fourth component for analysis[5][6], Lamei Zhang et al proposed a wire scattering model as the fifth component[7], Singh et al associated T_{13} and T_{23} with physical scattering mechanisms, the six-component scattering decomposition (6SD) and seven-component scattering (7SD) are presented [8][9], Wentao An used a modified reflection symmetry decomposition to improve the surface and double-bounce scattering powers[10].

Third model-based decomposition methods represent a combination of model-based decomposition and eigenvalue-based decomposition. Cloude made surface and double-bounce scattering models orthogonal to each other, aiming to minimize unknown variables[16]. The orientation angle compensation helps prevent negative values in the scattered powers, leading to the popular hybrid Freeman/eigenvalue decomposition technique. Singh et al. enhanced the initial hybrid Freeman/eigenvalue decomposition by utilizing distinct volume scattering models that were scattered from vegetation areas and oriented objects[17].

In this letter, we present an improved version of multiple components scattering decomposition for PolSAR data. Seven scattering models are used[9], i. e., surface scattering model, double-bounce scattering model, volume scattering model, helix scattering model, oriented dipole scattering model, compound dipole scattering model, and mixed dipole scattering model. Non-negative matrix factorization is achieved by limiting the volume scattered energy to obtain surface scattering and double bounce scattering energy. Additionally, the entropy obtained through eigenvalue decomposition of the coherency matrix enhanced the volume scattering power in vegetation areas. The improved version yields non-negative scattering powers and outperforms FDD, particularly when applied to vegetation areas.

This letter is organized as follows. The introduction is presented in Section I, and Section II is the proposed scattering models and the improved multiple-component scattering power decomposition. Experiments results on real PolSAR data are compared with several decomposition methods in Section III, and followed by the conclusions in Section IV.

II Modified Scattering Decomposition

Part A: Scattering Models

The multi-look data received in PolSAR systems using the {H, V} basis can be represented as a 3x3 complex matrix, which is also referred to as the coherency matrix. This matrix provides information about the polarization properties of the radar signal, including the phase and amplitude relationships between different polarization components. The coherency matrix of PolSAR image is presented as (1).

$$\langle T \rangle = \left\langle \vec{k}_p \cdot \vec{k}_p^{*t} \right\rangle = \begin{bmatrix} T_{11} & T_{12} & T_{13} \\ T_{12}^* & T_{22} & T_{23} \\ T_{13}^* & T_{23}^* & T_{33} \end{bmatrix} \tag{1}$$

In the PolSAR systems, k_p is a Pauli vector representing that represents single-look data. The angle brackets $\langle \cdot \rangle$ denote the mean of several observations from the objects within a resolution cell. As a result, $\langle T \rangle$ is a positive semidefinite Hermitian matrix.

Freeman and Durden developed the technique for PolSAR systems to break down the covariance matrix or the coherency matrix into three separate components. These three components consist of the surface scattering component, double-bounce scattering component, and volume scattering component[1]. Gulab Singh and his colleagues attributed physical scattering mechanisms to T_{23} and T_{13}, and established seven-component scattering decomposition (7SD) to provide an explanation for the coherency matrix of PolSAR data[9]. The scattering decomposition in this letter is demonstrated on the coherency matrix, and the coherency matrix is divided into seven parts as follows[9]:

$$\langle T \rangle = m_s T_s + m_d T_d + m_v T_v + m_h T_h + m_{md} T_{md} + m_{cd} T_{cd} + m_{od} T_{od} \tag{2}$$

where T_s, T_d, T_v, T_h, T_{md}, T_{cd} and T_{od} denote surface scattering model, double-bounce scattering model, volume scattering model, helix scattering model, oriented dipole scattering model, compound dipole scattering model, and mixed dipole scattering model respectively. Correspondingly, m_s, m_d, m_v, m_h, m_{md}, m_{cd}, and m_{od} represent

the corresponding scattering powers of seven submatrices.

T_s, T_d, T_v, T_h, T_{md}, T_{cd} and T_{od} are shown as follows[9]:

$$T_s = \frac{1}{|\beta|^2 + 1}\begin{bmatrix} 1 & \beta^* & 0 \\ \beta & |\beta|^2 & 0 \\ 0 & 0 & 0 \end{bmatrix} \tag{3}$$

$$T_d = \frac{1}{|\alpha|^2 + 1}\begin{bmatrix} 1 & \alpha^* & 0 \\ \alpha & |\alpha|^2 & 0 \\ 0 & 0 & 0 \end{bmatrix} \tag{4}$$

$$T_v = \frac{1}{4}\begin{bmatrix} 4 & 0 & 0 \\ 0 & 1 & 0 \\ 0 & 0 & 1 \end{bmatrix} \tag{5a}$$

$$T_v = \frac{1}{30}\begin{bmatrix} 15 & -5 & 0 \\ -5 & 7 & 0 \\ 0 & 0 & 8 \end{bmatrix} \tag{5b}$$

$$T_v = \frac{1}{30}\begin{bmatrix} 15 & 5 & 0 \\ 5 & 7 & 0 \\ 0 & 0 & 8 \end{bmatrix} \tag{5c}$$

$$T_v = \frac{1}{15}\begin{bmatrix} 0 & 0 & 0 \\ 0 & 7 & 0 \\ 0 & 0 & 8 \end{bmatrix} \tag{5d}$$

$$T_h = \frac{1}{2}\begin{bmatrix} 0 & 0 & 0 \\ 0 & 1 & \mp j \\ 0 & \pm j & 1 \end{bmatrix} \tag{6}$$

$$T_{md} = \frac{1}{2}\begin{bmatrix} 0 & 0 & 0 \\ 0 & 1 & \pm 1 \\ 0 & \pm 1 & 1 \end{bmatrix} \tag{7}$$

$$T_{cd} = \frac{1}{2}\begin{bmatrix} 1 & 0 & \pm j \\ 0 & 0 & 0 \\ \mp j & 0 & 1 \end{bmatrix} \tag{8}$$

$$T_{od} = \frac{1}{2}\begin{bmatrix} 1 & 0 & \pm 1 \\ 0 & 0 & 0 \\ \pm 1 & 0 & 1 \end{bmatrix} \tag{9}$$

where coefficient β in (3) sets $0 < \beta < 1$ and coefficient α in (4) is a complex value with $|\alpha| < 1$. T_v in (5a), (5b), (5c) and (5d) are the volume scattering models under different cases.

Part B: Modified Decomposition

This part presents an improved multiple components scattering decomposition for PolSAR data based on entropy H and anisotropy A. There two parameters are used to enhance the volume scattering power in vegetation areas with high-entropy. PolSAR data are divided into two categories, namely vegetation areas with high-entropy and other areas, then different decomposition techniques are adopted to obtain the better scattering powers. The vegetation areas' volume scattering powers have been improved while ensuring good performance in other areas.

According to the decomposition formula in (2) above and the model in (3) - (9), m_h and m_{md} can be calculated from T_{23}, while m_{cd} and m_{od} can be calculated from T_{13}. The solutions of are shown as:

$$m_h = 2\left|imag(T_{23})\right| \tag{10}$$

$$m_{md} = 2\left|real(T_{23})\right| \tag{11}$$

$$m_{cd} = 2\left|imag(T_{13})\right| \tag{12}$$

$$m_{od} = 2\left|real(T_{13})\right| \tag{13}$$

where $imag()$ in (10) and (12) denotes to get the imaginary part of an element and $real()$ in (11) and (13) denotes to get the real part of an element.

After removing the above four scattering powers from the coherency matrix, the residual part contains surface scattering power, double-bounce scattering power, volume scattering power shown as (14), and the residual part $\langle T^{re}\rangle$ is shown as (15).

$$\langle T^{re}\rangle = m_s T_s + m_d T_d + m_v T_v = \langle T\rangle - m_h T_h - m_{md} T_{md} - m_{cd} T_{cd} - m_{od} T_{od} \tag{14}$$

$$\langle T^{re}\rangle = \begin{bmatrix} T_{11}^{re} & T_{12}^{re} & T_{13}^{re} \\ T_{12}^{re*} & T_{22}^{re} & T_{23}^{re} \\ T_{13}^{re*} & T_{23}^{re*} & T_{33}^{re} \end{bmatrix} \tag{15}$$

Each element in T_{re} is represented as follows:

$$T_{11}^{re} = T_{11} - \frac{1}{2}m_{cd} - \frac{1}{2}m_{od} = T_{11} - \left|imag\left(T_{13}\right)\right| - \left|real(T_{13})\right| \tag{16}$$

$$T_{22}^{re} = T_{22} - \frac{1}{2}m_h - \frac{1}{2}m_{md} = T_{22} - \left|imag\left(T_{23}\right)\right| - \left|real(T_{23})\right| \tag{17}$$

$$T_{33}^{re} = T_{33} - \frac{1}{2}m_h - \frac{1}{2}m_{md} - \frac{1}{2}m_{cd} - \frac{1}{2}m_{od} = T_{33} - \left|imag\left(T_{23}\right)\right| - \left|real(T_{23})\right| - \left|imag\left(T_{13}\right)\right| - \left|real(T_{13})\right| \tag{18}$$

$$T_{12}^{re} = T_{12} \tag{19}$$

$$T_{13}^{re} = T_{13} \pm \frac{1}{2}m_{cd}j \pm \frac{1}{2}m_{od} = T_{13} - imag\left(T_{13}\right)j - real\left(T_{13}\right) = 0 \tag{20}$$

$$T_{23}^{re} = T_{23} \mp \frac{1}{2}m_h j \pm \frac{1}{2}m_{md} = T_{23} - imag\left(T_{23}\right)j - real(T_{23}) = 0 \tag{21}$$

To guarantee that the three scattering powers i. e., m_s, m_d and m_v from $\langle T^{re}\rangle$ are positive, it is necessary to ensure that T_{11}^{re}, T_{22}^{re} and T_{33}^{re} are all positive. However, there may be certain pixels where these values are less than zero. In these instances, m_h, m_{md}, m_{cd} and m_{od} must be modified appropriately to ensure that T_{11}^{re}, T_{22}^{re} and T_{33}^{re} remain non-negative. If $T_{33}^{re}<0$, gradually reduce m_h, m_{md}, m_{cd} and m_{od} at the same time until $T_{33}^{re}>=0$ is satisfied. Then, if T_{11}^{re} is still less than 0, set m_{cd}=0 and m_{od}= 0. Similarly, if T_{22}^{re} is still less than 0, set m_h=0 and m_{md} =0.

After obtaining the values of m_h, m_{md}, m_{cd} and m_{od} through the above solution, in order to calculate the value of m_s, m_d and m_v, T_{13}^{re} and T_{23}^{re} which are not equal to 0

in some pixels were ignored and the residual matrix $\langle T^{re}\rangle$ is set to the following form as (22) and (23).

$$\langle T^{re}\rangle = \begin{bmatrix} T_{11}^{re} & T_{12}^{re} & 0 \\ T_{12}^{re*} & T_{22}^{re} & 0 \\ 0 & 0 & T_{33}^{re} \end{bmatrix} \tag{22}$$

$$\langle T^{re}\rangle = m_s T_s + m_d T_d + m_v T_v \tag{23}$$

To determine the volume scattering power m_v, it is first necessary to determine whether volume scattering is from the dihedral structure or the dipole structure. Set $C_1 = T_{11}^{re} - T_{22}^{re}$, such that, if $C_1 < 0$, the volumetric scattering model T_v is shown as (5d), and if $C_1 \geqslant 0$, the volumetric scattering model T_v is shown as one of (5a), (5b) and (5c). By utilizing the co-polarized ratio R (24), one can determine the suitable model for volumetric scattering. The detailed steps are as follows: if $|R| \leqslant 2$, the volumetric scattering model T_v is in (5a); if $R > 2$, T_v is in (5b); if $R < -2$, T_v is in (5c)[3]. The solutions for volume scattering power m_v under various scenarios are expressed as equation (25).

$$R = 10log\left(\frac{|S_{VV}|^2}{|S_{HH}|^2}\right) = 10log\left(\frac{T_{11}^{re} + T_{22}^{re} - 2real(T_{12}^{re})}{T_{11}^{re} + T_{22}^{re} + 2real(T_{12}^{re})}\right) \tag{24}$$

$$m_v = \begin{cases} 4T_{33}^{re} & if\left(T_{11}^{re} - T_{22}^{re}\right) \geqslant 0 \ and \ |R| \leqslant 2 \\ \dfrac{30}{8}T_{33}^{re} & if\left(T_{11}^{re} - T_{22}^{re}\right) \geqslant 0 \ and \ R > 2 \\ \dfrac{30}{8}T_{33}^{re} & if\left(T_{11}^{re} - T_{22}^{re}\right) \geqslant 0 \ and \ R < -2 \\ \dfrac{15}{8}T_{33}^{re} & if\left(T_{11}^{re} - T_{22}^{re}\right) < 0 \end{cases} \tag{25}$$

After subtracting the volume scattering part from $\langle T^{re}\rangle$ denoted by $\langle T^{sd}\rangle$ shown in (26), $\langle T^{sd}\rangle$ consists of surface scattering part and double-bounce scattering part and the different cases of the volume scattering are shown in equation (27).

$$\langle T^{sd}\rangle = m_s T_s + m_d T_d = \langle T^{re}\rangle m_v T_v = \begin{bmatrix} T_{11}^{sd} & T_{12}^{sd} & 0 \\ T_{12}^{sd*} & T_{22}^{sd} & 0 \\ 0 & 0 & 0 \end{bmatrix} \tag{26}$$

$$\langle T^{sd}\rangle = \begin{cases} \begin{bmatrix} T_{11}^{re} - \frac{1}{2}m_v & T_{12}^{re} & 0 \\ T_{12}^{re*} & T_{22}^{re} - \frac{1}{4}m_v & 0 \\ 0 & 0 & 0 \end{bmatrix} & if\ T_v \text{ is (5a)} \\ \begin{bmatrix} T_{11}^{re} - \frac{1}{2}m_v & T_{12}^{re} + \frac{1}{6}m_v & 0 \\ T_{12}^{re*} + \frac{1}{6}m_v & T_{22}^{re} - \frac{7}{8}m_v & 0 \\ 0 & 0 & 0 \end{bmatrix} & if\ T_v \text{ is (5b)} \\ \begin{bmatrix} T_{11}^{re} - \frac{1}{2}m_v & T_{12}^{re} - \frac{1}{6}m_v & 0 \\ T_{12}^{re*} - \frac{1}{6}m_v & T_{22}^{re} - \frac{7}{8}m_v & 0 \\ 0 & 0 & 0 \end{bmatrix} & if\ T_v \text{ is (5c)} \\ \begin{bmatrix} T_{11}^{re} & T_{12}^{re} & 0 \\ T_{12}^{re*} & T_{22}^{re} - \frac{7}{8}m_v & 0 \\ 0 & 0 & 0 \end{bmatrix} & if\ T_v \text{ is (5d)} \end{cases} \tag{27}$$

The volume scattering power m_v is shown as (25), and the surface scattering power m_s and double-bounce scattering power m_d are the eigenvalues of $\langle T^{sd}\rangle$. The eigenvalue decomposition is $\langle T^{sd}\rangle$ shown as (28).

$$\langle T^{sd}\rangle = \lambda_1 k_1 {k_1^t}^* + \lambda_2 k_2 {k_2^t}^* \tag{28}$$

$$k_i = \begin{bmatrix} cos\alpha_i \\ sin\alpha_i cos\beta_i e^{j\delta_i} \\ 0 \end{bmatrix} \tag{29}$$

where λ_1 and λ_2 is the eigenvalues, and k_1 and k_2 are the corresponding eigenvectors shown in (29) with $\alpha_1 + \alpha_2 = 90^\circ$. According to reference [17], when the scattering mechanism angles $\alpha_1 + \alpha_2 = 90^\circ$, it can be considered that the surface scattering model and the double-bounce scattering model derived from the eigenvectors space of the coherency matrix. The specific situations are as follows: if $\alpha_1 \leqslant 45^\circ$, then $T_s = k_1 {k_1^t}^*$ and $T_d = k_2 {k_2^t}^*$; if $\alpha_1 > 45^\circ$, then $T_s = k_2 {k_2^t}^*$, and $T_d = k_1 {k_1^t}^*$. The surface scattering power m_s and double-bounce scattering power m_d can be solved as (30).

$$\begin{cases} m_s = \lambda_1 \\ m_d = \lambda_2 \end{cases} \text{If } \alpha_1 \leqslant 45^\circ \qquad \begin{cases} m_s = \lambda_2 \\ m_d = \lambda_1 \end{cases} \text{If } \alpha_1 > 45^\circ \tag{30}$$

If some λ_1 or λ_2 of $\langle T^{sd}\rangle$ is less than zero, we can gradually reduce m_v until $\lambda_1 \geqslant 0$ and $\lambda_2 \geqslant 0$ are satisfied. Then, use (30) to calculate surface scattering power m_s and double-bounce scattering power m_d.

In order to obtain non-negative eigenvalues λ_1 and λ_2, we reduce the volume scattering power m_v, which usually leads to an underestimation of m_v, especially in high-entropy regions. To deal with this situation, we adjusted the calculation method of volume scattering power m_v in high-entropy regions. We consider that $\langle T^{sd}\rangle$ of high-entropy regions consists of double-bounce scattering

and volume scattering, and the surface scattering is not included.

Entropy of the coherency matrix is calculated as (31)[15]. p_i in (32) is the normalized eigenvalue λ_i of the coherency matrix $\langle T \rangle$. Entropy represents the degree of randomness of the targets in a cell. When entropy is equal to 1, it means that the current target is completely random and usually belongs to the vegetation areas. When entropy equals zero, it means that the target is not random at all and is a deterministic target, which usually belongs to the rough surface areas.

$$H = -\sum_{i=1}^{3} p_i \cdot log_3 p_i \tag{31}$$

$$p_i = \frac{\lambda_i}{\lambda_1 + \lambda_2 + \lambda_3}, \quad i\epsilon\{1, 2, 3\} \tag{32}$$

$$A = \frac{\lambda_2 - \lambda_3}{\lambda_2 + \lambda_3} \tag{33}$$

The anisotropy A in (33) indicates the degree of heterogeneity of the target. In PolSAR images, anisotropy A is usually used in conjunction with entropy H[15]. When the entropy H is high, anisotropy A is used to distinguish whether the target belongs to vegetation areas or artificial areas. In addition to the volume scattering power obtained by the calculation in (25), we believe that part of volume scattering power exists in the matrix $\langle T^{sd} \rangle$ in some entropy high case. When $H - A > 0.4$, we consider that the current target belongs to the vegetation areas, the calculation of m_s, m_d, and the additional m_v is shown as follows:

$$\begin{cases} m_s = 0 \\ m_d = \lambda_2 \quad \text{If } \alpha_1 \leqslant 50^\circ \\ m_v = \lambda_1 \end{cases} \qquad if\ H - A > 0.4 \tag{34}$$

$$\begin{cases} m_s = 0 \\ m_d = \lambda_1 \quad \text{If } \alpha_1 > 50^\circ \\ m_v = \lambda_2 \end{cases}$$

The flowchart of modified multiple-component scattering power decomposition for the original coherency matrix of the PolSAR data is shown in Figure 1.

In this letter, the orientation angle compensation (OAC) can be used on the modified decomposition method. The rotation matrices are shown in (35) and (36). The coherency matrices are shown as (37) and (38) after two OACs. To reduce T_{33} and $T_{33}(\theta)$, the value of θ and φ can be solved as shown in (39) and (40) respectively.

$$R(\theta) = \begin{bmatrix} 1 & 0 & 0 \\ 0 & \cos 2\theta & \sin 2\theta \\ 0 & -\sin 2\theta & \cos 2\theta \end{bmatrix} \tag{35}$$

$$U(\varphi) = \begin{bmatrix} 1 & 0 & 0 \\ 0 & \cos 2\varphi & j\sin 2\varphi \\ 0 & j\sin 2\varphi & \cos 2\varphi \end{bmatrix} \tag{36}$$

$$\langle T(\theta) \rangle = R(\theta) \langle T \rangle R(\theta)' \tag{37}$$

$$\langle T(\varphi) \rangle = U(\varphi) \langle T(\theta) \rangle U(\varphi)' \tag{38}$$

$$\theta = \frac{1}{4}\tan^{-1}\left(\frac{2\,\mathrm{real}(T_{23})}{T_{22} - T_{33}}\right) + \frac{n\pi}{4}, \quad n = 0, \pm 1 \tag{39}$$

$$\varphi = \frac{1}{4}\tan^{-1}\left(\frac{2\,\mathrm{imag}(T_{23}(\theta))}{T_{22}(\theta) - T_{33}(\theta)}\right) + \frac{m\pi}{4}, \quad m = 0, \pm 1 \tag{40}$$

After the first OAC by $R(\theta)$, $real(T_{23}(\theta)) = 0$, according to (11), $m_{md} = 0$. The proposed method has become six-component scattering power decomposition. After the second OAC by $U(\varphi)$, $T_{23}(\varphi) = 0$, according to (10), $m_h = 0$. The proposed method has become five-component scattering power decomposition.

III Experiments Results

To demonstrate the effectiveness of the proposed Freeman/Eigenvalue decomposition, various experiments were conducted using fully PolSAR data. This is a L-band 4-look AIRSAR dataset on San Francisco. The resolution is 10m×10m, the incidence angle of the radar is 5°~60°, the size of selected image is 700×600 pixels. The data is on {H, V} base, and the diagonal elements of the coherence matrix form a color image with T_{11} as blue, T_{22} as red, and T_{33} as green, shown as Figure 2. The three areas with red rectangular in the Figure 2 are used for subsequent experimental demonstrations, and they are called zone1, zone2, and zone3, from top to bottom. The respective terrain labels of zone1, zone2, and zone3 are ocean areas, urban areas and vegetation areas.

Three decomposition algorithms are chosen to compare and demonstrate the results of the proposed decomposition (PD) in this letter, including the Freeman-Durden scattering matrix power decomposition (FDD)[1] using three volume scattering models (volume scattering models are shown in (5a), (5b), and (5c)), Yamaguchi four-component scattering matrix power decomposition (Y4D)[3], seven-component scattering matrix power decomposition (7SD) [9]. Figure 3, Figure 4, and Figure 5 display the decomposition results of the AIRSAR data. In these figures, surface scattering power m_s is used for blue, double-bounce scattering power m_d is used for red, and volume scattering power m_v is used for green. Figure 3 displays the decomposition results of the original coherency matrix of the AIRSAR data without OAC. Figure 4 displays the decomposition results of the coherency matrix with the OAC by using $R(\theta)$. Figure 5 displays the decomposition results of the coherency matrix with two kinds of OAC by using $R(\theta)$ and $U(\varphi)$ successively.

As can be seen from Figure 3, Figure 4, and Figure 5, the four decomposition algorithms can preserve the important features of the AIRSAR data by extracting the three main scattering powers m_s, m_d, and m_v. In Figure 3 (c), Figure 4(c), and Figure 5(c), it can be observed that 7SD performs better for urban areas, with colors trending towards red. This indicates a larger proportion of double-bounce scattering power in urban areas. In Figure 3(d), Figure 4(d), and Figure 5(d), it can be seen that the PD shows a reddish color for urban areas, indicating a larger proportion of double-bounce scattering

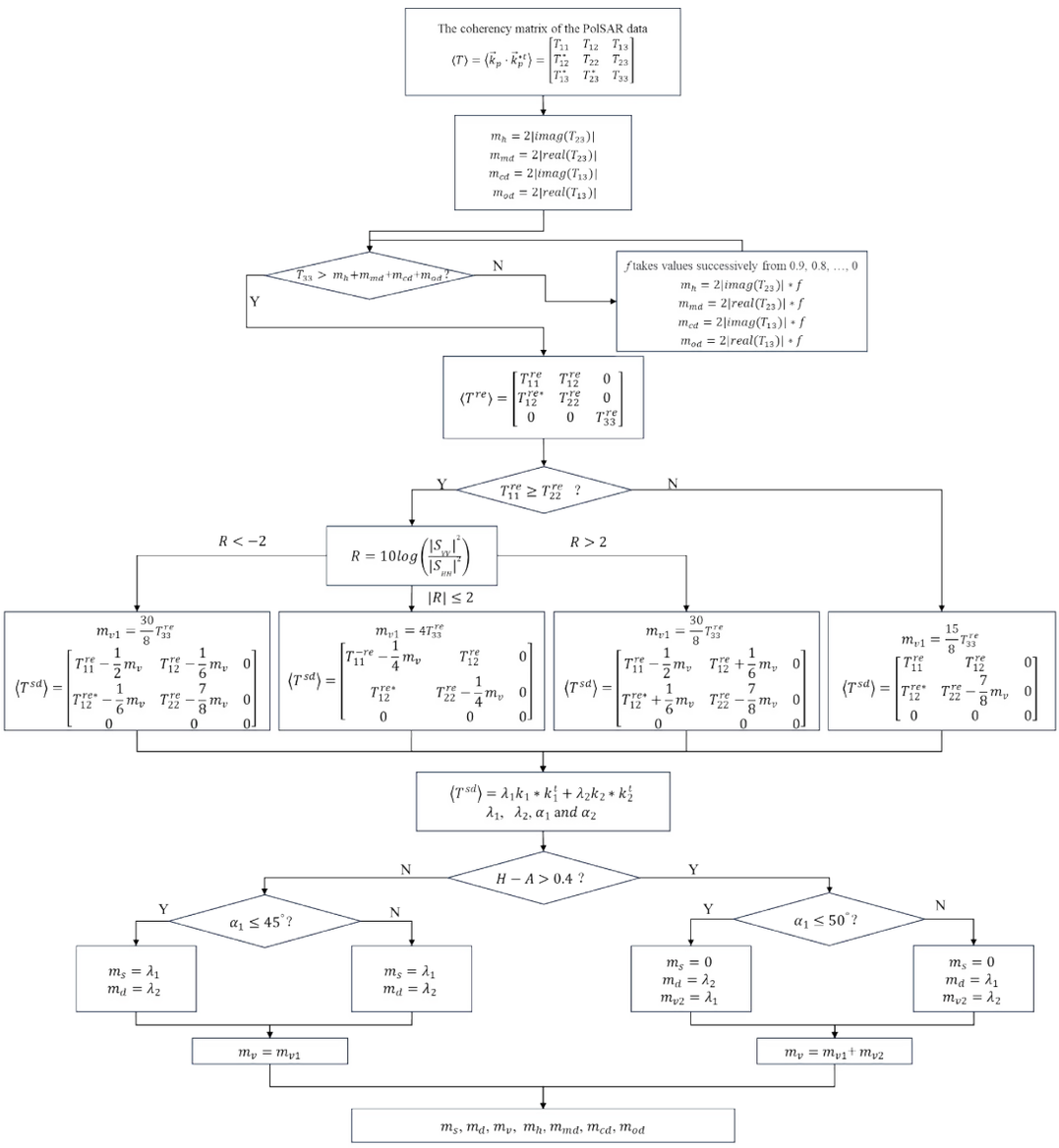

Figure 1 Flowchart of modified multiple-component scattering power decomposition
图1 改进的多元散射能量分解方法流程图

power. The vegetation areas tend towards green, indicating a larger proportion of volume scattering power in vegetation areas.

To visually demonstrate the effectiveness of the proposed algorithm in scattering powers, the scattering power of the original coherency matrix of the AIRSAR data without OAC are represented in Figure 6~8. The scattering power is shown a grayscale image, where black indicates a 0% proportion and white indicates a 100% proportion in terms of total power. Based on Figure 6, Figure 7 and Figure 8, it can be concluded that all of the four decomposition algorithms can obtain higher surface scattering powers over the ocean areas, the double-bounce scattering powers are strongest in urban areas and the volume scattering powers are strongest in vegetation areas. In Figure 8, the PD not only ensures the largest volume scattering power of vegetation areas but also minimizes the volume scattering power in urban areas and ocean areas.

Quantitative comparison is made using the three zones in Figure 2. The scattering powers from these decomposition algorithms for the original coherency matrices without OAC in zone1, zone2, and zone3 are displayed in Table 1, Table 2, and Table 3, respectively.

From Table 1, Table 2, and Table 3, it can be seen that compared with the other three algorithms, the proportion of surface scattering power of PD algorithm in zone1 is as high as 93.64%, only slightly inferior to Y4D. In zone2, PD algorithm has the highest proportion of double-bounce scattering power, while 7SD algorithm focuses its power on double-bounce scattering, mixed dipole scattering and surface scattering. PD algorithm concentrates its power on double-bounce scattering, surface scattering, and mixed dipole scattering sequentially. This phenomenon is consistent with the possible scattering types that may occur in urban areas. In zone3, PD al-

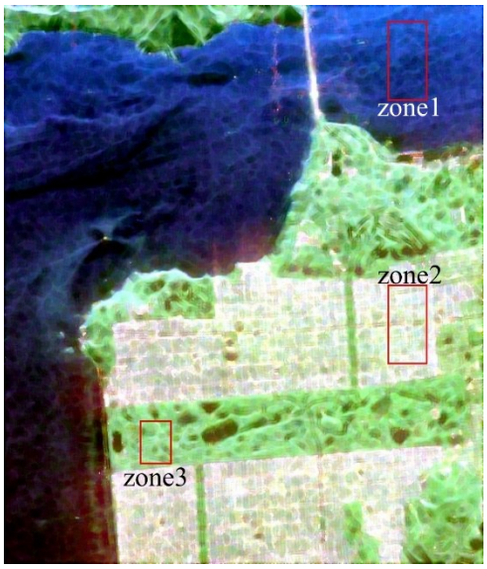

Figure 2 Original Image
图2 原图

gorithm obtains the highest volume scattering power, accounting for as much as 90.41%. Because the PD algorithm has improved using entropy to decompose the coherency matrix. If entropy H is high and anisotropy A is low, i. e., $H - A > 0.4$, it considers that surface scattering does not exist, and the scattering power with scattering angle less than 50° is classified as volume scattering, which increases the volume scattering power.

The scattering powers from these decomposition algorithms for the coherency matrices with OAC by using $R(\theta)$ in zone1, zone2, and zone3 are displayed in Table 4, Table 5, and Table 6, respectively. Because after OAC $R(\theta)$, $m_{md} = 0$, so PD and 7SD both have six scattering powers. In zone1 (shown in Table 4), the proportion of surface scattering power of PD algorithm is as high as 93.96%, only slightly inferior to Y4D. These four algorithms obtain higher proportion of surface scattering power than 92%. In zone2 (shown in Table 5), the double-bounce scattering power of PD algorithm is the highest one, and it is 50.06%. In zone3 (shown in Table 6), PD algorithm gets the highest volume scattering power, which is 88.58%. It is 1.51%, 14.89% and 40.32% higher than FDD, Y4D and 7SD respectively.

The scattering powers from these decomposition algorithms for the coherency matrices with two kinds of OAC by using $R(\theta)$ and $U(\varphi)$ successively in zone1, zone2, and zone3 are displayed in Table 4, Table 5, and Table 6, respectively. Because after OAC by $R(\theta)$ and $U(\varphi)$, $m_{md} = 0$ and $m_h = 0$, so PD and 7SD both have five scattering powers. In zone1 (shown in Table 7), the

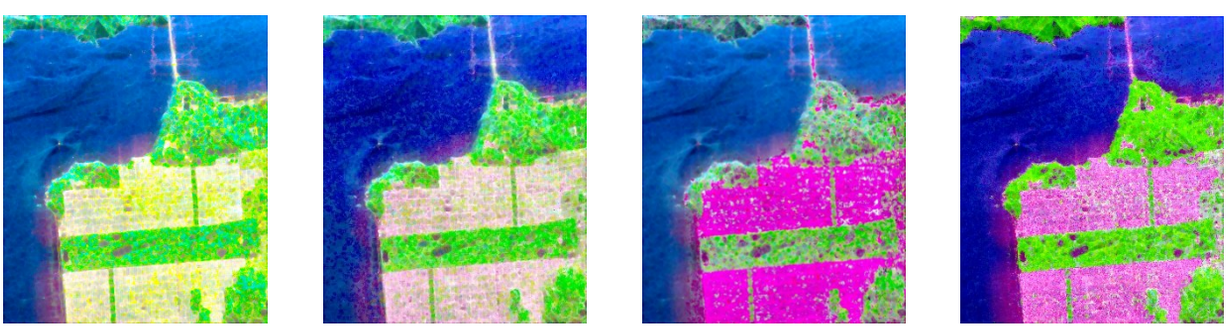

(a) FDD (b) Y4D (c) 7SD (d) PD

Figure 3 Decomposition results for the coherency matrix
图3 相干矩阵的分解结果

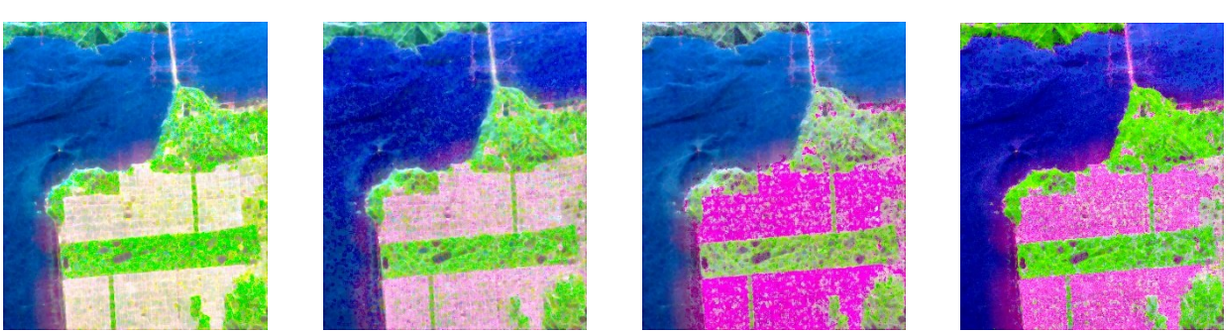

(a) FDD (b) Y4D (c) 7SD (d) PD

Figure 4 Decomposition results for the coherency matrix with OAC by $R(\theta)$
图4 Rθ方位角补偿后的相干矩阵的分解结果

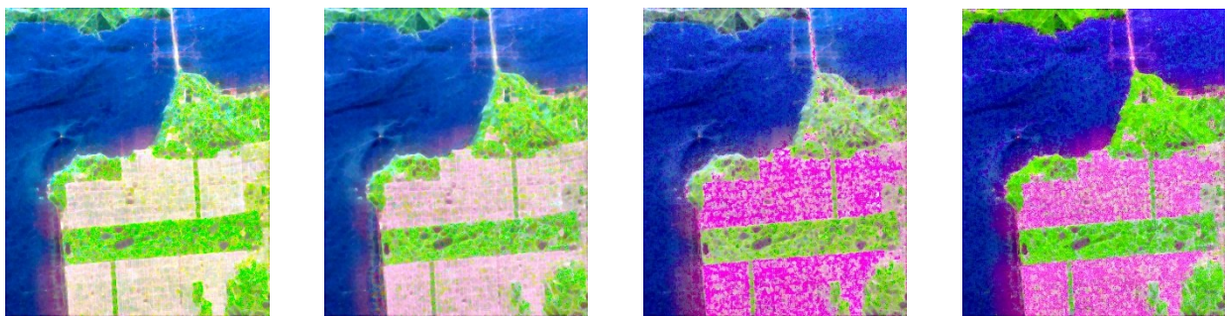

（a） FDD （b） Y4D （c） 7SD （d） PD

Figure 5 Decomposition results for the coherency matrix with OAC by $R(\theta)$ and $U(\varphi)$
图5 Rθ 和 Uφ方位角补偿后的相干矩阵的分解结果

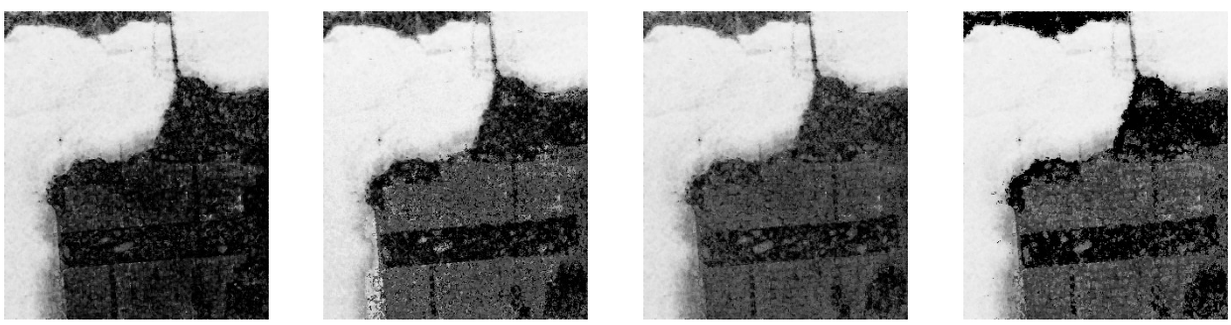

（a） FDD （b） Y4D （c） 7SD （d） PD

Figure 6 Surface scattering powers of the coherency matrix
图6 相干矩阵的表面散射能量

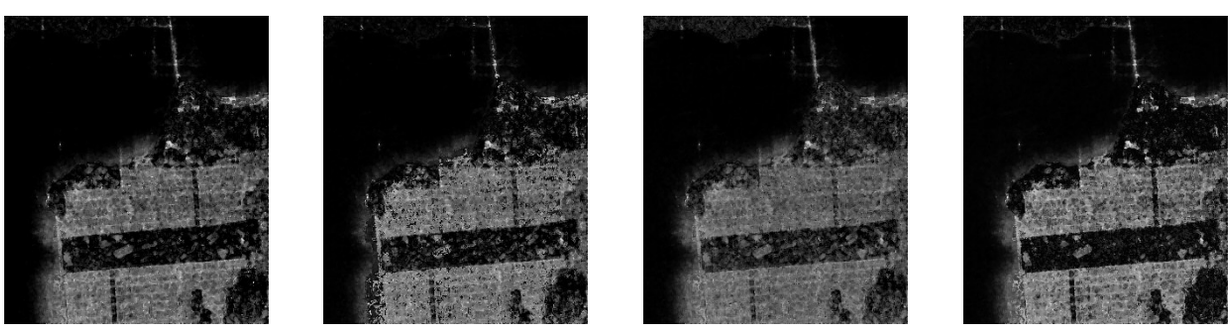

（a） FDD （b） Y4D （c） 7SD （d） PD

Figure 7 Double-bounce scattering powers of the coherency matrix
图7 相干矩阵的二次散射能量

proportion of surface scattering power of PD algorithm is as high as 95.17%, only slightly inferior to FDD. These four algorithms obtain higher proportion of surface scattering power than 93%. Compared with Table 4, double-bounce scatting power is a slight improvement. In zone2 (shown in Table 8), the double-bounce scattering power of PD algorithm is the highest one, and it is 51.77%. In zone3 (shown in Table 9), PD algorithm gets the highest volume scattering power, which is 87.30%. It is 3.77%, 10.21% and 32.44% higher than FDD, Y4D and 7SD respectively. Compared with Table 6 and Table 3, although there is a slight decrease in volume scattering in Table 9, the volume scattering still occupies an absolute dominant position.

IV Conclusion

This letter proposed a modified multiple-component scattering power decomposition. This paper combines eigenvalue decomposition with model decomposition. Re-

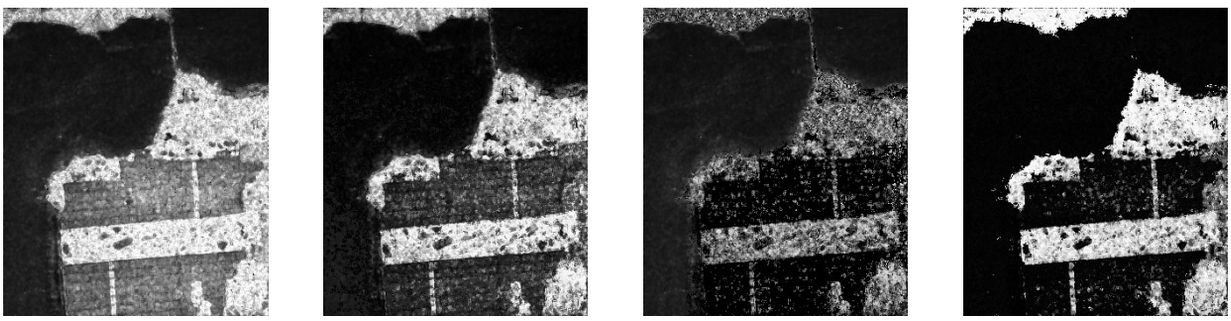

（a） FDD （b） Y4D （c） 7SD （d） PD

Figure 8 Volume scattering powers of the coherency matrix
图8 相干矩阵的体散射能量

Table 1 Scattering powers in zone1 for $\langle T \rangle$ (%)
表1 相干矩阵T区域1的散射能量(%)

Method / Powers	FDD	Y4D	7SD	PD
$\boldsymbol{m_s}$	**91.62**	**94.21**	**91.85**	**93.64**
m_d	0.01	0.18	0.25	0.95
m_v	8.36	3.02	7.91	2.60
m_h	——	2.59	0	0.28
m_{md}	——	——	0	0.10
m_{od}	——	——	0	1.16
m_{cd}	——	——	0	1.26

Table 2 Scattering powers in zone2 for $\langle T \rangle$ (%)
表2 相干矩阵T区域2的散射能量(%)

Method / Powers	FDD	Y4D	7SD	PD
m_s	13.21	30.41	25.81	32.90
$\boldsymbol{m_d}$	35.41	**37.82**	**32.75**	**40.51**
m_v	**51.38**	26.50	6.51	7.03
m_h	——	5.27	3.59	1.95
m_{md}	——	——	18.36	8.98
m_{od}	——	——	9.98	5.78
m_{cd}	——	——	3.02	2.85

Table 3 Scattering powers in zone3 for $\langle T \rangle$ (%)
表3 相干矩阵T区域3的散射能量(%)

Method / Powers	FDD	Y4D	7SD	PD
m_s	3.15	7.09	15.97	2.96
m_d	7.07	9.14	15.17	6.53
$\boldsymbol{m_v}$	**89.77**	**79.12**	**44.92**	**90.41**
m_h	——	4.65	4.46	0.02
m_{md}	——	——	5.38	0.02
m_{od}	——	——	7.11	0.02
m_{cd}	——	——	6.99	0.04

ferring to 7SD[9], this letter adopts seven scattering models. Entropy and anisotropy are used to get the volume scattering power. The effectiveness of the proposed algorithm in this letter has been demonstrated by experiments on the real PolSAR data, especially in vegetation areas.

Table 4 Scattering powers in zone1 for $\langle T(\theta) \rangle$ (%)
表4 相干矩阵Tθ区域1的散射能量(%)

Method / Powers	FDD	Y4D	7SD	PD
$\boldsymbol{m_s}$	**92.07**	**94.67**	**92.26**	**93.96**
m_d	0.07	0.15	0.29	1.00
m_v	7.91	2.61	7.44	2.34
m_h	——	2.57	0	0.34
m_{od}	——	——	0	0.64
m_{cd}	——	——	0	1.73

Table 5 Scattering powers in zone2 for $\langle T(\theta) \rangle$ (%)
表5 相干矩阵Tθ区域2的散射能量(%)

Method / Powers	FDD	Y4D	7SD	PD
m_s	19.58	34.61	28.45	31.04
$\boldsymbol{m_d}$	**43.35**	**43.37**	**47.51**	**50.06**
m_v	37.08	17.03	3.39	4.89
m_h	——	4.99	4.80	2.80
m_{od}	——	——	10.14	7.27
m_{cd}	——	——	5.71	3.94

Table 6 Scattering powers in zone3 for $\langle T(\theta) \rangle$ (%)
表6 相干矩阵Tθ区域3的散射能量(%)

Method / Powers	FDD	Y4D	7SD	PD
m_s	3.79	9.06	13.58	4.49
m_d	10.14	12.60	19.46	6.84
$\boldsymbol{m_v}$	**86.07**	**73.69**	**48.26**	**88.58**
m_h	——	4.65	4.59	0.02
m_{od}	——	——	7.83	0.02
m_{cd}	——	——	6.29	0.05

Table 7 Scattering powers in zone1 for $\langle T(\varphi)\rangle$ (%)
表7 相干矩阵Tφ区域1的散射能量(%)

Method / Powers	FDD	Y4D	7SD	PD
$\boldsymbol{m_s}$	**94.08**	**93.95**	**94.52**	**95.17**
m_d	0.19	0.67	1.01	1.33
m_v	5.74	5.38	3.45	1.34
m_{od}	——	——	0.62	1.33
m_{cd}	——	——	0.41	0.82

Table 8 Scattering powers in zone2 for $\langle T(\varphi)\rangle$ (%)
表8 相干矩阵Tφ区域2的散射能量(%)

Method / Powers	FDD	Y4D	7SD	PD
m_s	20.15	32.73	29.26	30.04
$\boldsymbol{m_d}$	**43.93**	**45.83**	**50.19**	**51.77**
m_v	35.92	21.44	4.62	5.23
m_{od}	——	——	10.11	8.36
m_{cd}	——	——	5.81	4.60

Table 9 Scattering powers in zone3 for $\langle T(\varphi)\rangle$ (%)
表9 相干矩阵Tφ区域3的散射能量(%)

Method / Powers	FDD	Y4D	7SD	PD
m_s	4.34	8.05	10.55	5.31
m_d	12.13	14.86	21.01	7.31
$\boldsymbol{m_v}$	**83.53**	**77.09**	**54.86**	**87.30**
m_{od}	——	——	7.29	0.02
m_{cd}	——	——	6.29	0.05

References

[1] *A. Freeman*, S. L. Durden, "A three-component scattering model for polarimetric SAR data," IEEE Transactions on geoscience and remote sensing, 1998, **36**(3): 963-973.

[2] *F. Xu*, Y.-Q. Jin, "Deorientation theory of polarimetric scattering targets and application to terrain surface classification," IEEE Transactions on geoscience and remote sensing, 2005, **43**(10): 2351-2364.

[3] Y. Yamaguchi, A. Sato, W.-M. Boerner, R. Sato, and H. Yamada, "Four-component scattering power decomposition with rotation of coherency matrix," *IEEE Transactions on geoscience and remote sensing*, 2011, **49**(6): 2251-2258.

[4] G. Singh, Y. Yamaguchi, and S.-E. Park, "General four-component scattering power decomposition with unitary transformation of coherency matrix," *IEEE Transactions on geoscience and remote sensing*, 2013, **51**(5): 3014-3022.

[5] Y. Yamaguchi, T. Moriyama, M. Ishido, and H. Yamada, "Four-component scattering model for polarimetric SAR image decomposition," *IEEE Transactions on Geoscience and Remote Sensing*, 2005, **43**(8): 1699-1706.

[6] A. Sato, Y. Yamaguchi, G. Singh, and S.-E. Park, "Four-component scattering power decomposition with extended volume scattering model," *IEEE Geoscience and Remote Sensing Letters*, 2012, **9**(2): 166-170.

[7] L.-M. Zhang, B. Zou, H.-J. Cai, and Y. Zhang. "*Multiple-component scattering model for polarimetric SAR image decomposition*," IEEE Geoscience and Remote Sensing Letters, 2008, **5**(4): 603-607.

[8] *G. Singh*, and Y. Yamaguchi, "Model-based six-component scattering matrix power decomposition. IEEE Transactions on Geoscience and Remote Sensing," 2018, (**56**)10: 5687-5704.

[9] G. Singh, R. Malik, S. Mohanty, V.-S. Rathore, K. Yamada, M. Umemura, and Y. Yamaguchi, "Seven-component scattering power decomposition of POLSAR coherency matrix," *IEEE Transactions on Geoscience and Remote Sensing*, 2019, **57**(11): 8371-8382.

[10] *W. An*, M. Lin, H. Yang, "Modified reflection symmetry decomposition and a New polarimetric product of GF-3," IEEE Geoscience and Remote Sensing Letters, 2022, 19, 8019805, 2022.

[11] H. Li, Q. Li, G. Wu, J. Chen, and S. Liang, "Adaptive two-component model-based decomposition for polarimetric SAR data without assumption of reflection symmetry", *IEEE Transactions on Geoscience and Remote Sensing*, 2017, **55**(1): 197-211.

[12] D. Xiang, W. Wang, T. Tang, and Y. Su, "Multiple-component polarimetric decomposition with new volume scattering models for PolSAR urban areas," *IET Radar*, Sonar & Navigation, 2017, **11**(3): 410-419.

[13] V. Turkar, J. Checker, S. De, G. Singh, "*Impact of G4U and 7-component target decomposition on PolSAR image semantic segmentation*," *Advances in Space Research*, 2022, **70**(12): 3798-3810.

[14] W. Han, H. Fu, J. Zhu, C. Wang, and Q. Xie, "Polarimetric SAR decomposition by incorporating a rotated dihedral scattering model," *IEEE Geoscience and Remote Sensing Letters*, 2022, 19:4005505.

[15] *S. R. Cloude*, and E. Pottier, "An entropy based classification scheme for land applications of polarimetric SAR," IEEE Transactions on Geoscience and Remote Sensing, 1997, **35**(1): 68-78.

[16] S. R. Cloude. Polarisation: Applications in Remote Sensing. London, U.K.: Oxford Univ. Press, 2009.

[17] G. Singh, Y. Yamaguchi, and S. E. Park, "Hybrid Freeman/eigenvalue decomposition method with extended volume scattering model," *IEEE Geoscience Remote Sensing Letters*, 2013, **10**(1): 81-83.

[18] B. Sun, W. Tan, W. Xu, P. Huang, "An improved hybrid Freeman/eigenvalue decomposition for polarimetric SAR data," *2019 IEEE International Conference on Signal*, Information and Data Processing (ICSIDP), 2019: 19892107.

[19] S. Zhang, X.-C. Yu, and L, *Wang*, "*Modified version of three-component model-based decomposition for polarimetric SAR data*," *Journal of Systems Engineering and Electronics*, 2019, **30**(2): 270-277.

[20] G. Singh, Y. Yamaguchi, and S. E. Park, "Generalized hybrid model-based/eigenvalue decomposition," *2013 Asia-Pacific Conference on Synthetic Aperture Radar (APSAR)*, 2013: 14026506.

[21] J.-J. van Zyl, Y. Kim, M. Arii, "Requirements for model-based polarimetric Decompositions," *2008 IEEE International Geoscience and Remote Sensing Symposium*, 2008: 10472722.

[22] J.-J. van Zyl, M. Arii, and Y. Kim, "Model-Based decomposition of polarimetric SAR covariance matrices constrained for nonnegative eigenvalues," *IEEE Transactions on Geoscience and Remote Sensing*, 2011, **49**(9): 3452-3459.